

# CIMAR-5: A Snapshot of the Lower Troposphere over the Subtropical Southeast Pacific



René D. Garreaud,\* José Rutllant,\* Juan Quintana,+  
Jorge Carrasco,+ and Patrick Minnis#

## ABSTRACT

The extensive and persistent deck of stratocumulus (SCu) off the west coast of subtropical South America plays an important role in the regional and global climate, as well as in coastal weather. As in other subtropical regions, the SCu form at the top of a marine boundary layer (MBL) bounded by a relatively cold ocean and a large-scale subsidence inversion. Nevertheless, details of the structure and variability of the lower troposphere over this region are largely unknown. Ship-based meteorological observations taken along a transect at 27°S from the Chilean coast (71°W) to Easter Island (110°W) during the second half of October 1999 provide a preliminary description of the low-level circulation, thermodynamic structure, and cloudiness over the subtropical southeast Pacific. Three types of observations were made: (a) 15-min average of air temperature, relative humidity, solar radiation, pressure, and wind by an automatic weather station on the ship deck; (b) 15-min average of vertical reflectivity and cloud base by a laser ceilometer on the ship deck; and (c) twice-daily rawinsondes. Several cloud and radiation properties were derived from *GOES-8* imagery and validated against the ship-based observations. A preliminary assessment of the ability of NCEP–NCAR reanalysis and scatterometer winds in representing the atmosphere over a largely in situ data-void area is also presented.

Sea surface temperature and near-surface air temperature increase gradually westward, while near-surface relative humidity remains nearly constant at ~80%. A significant increase in the free-tropospheric moisture indicates an offshore decrease in the large-scale subsidence. Consistently, the MBL evolves from a shallow, well-mixed MBL topped by compact SCu near the coast; to a deeper, decoupled MBL with a cumuli rising into a patchy SCu deck near Easter Island, in a similar fashion to the transition from subtropical-stratus regime to trade-cumulus regime described elsewhere. In addition to these “climatological” features, the ship data also reveal the large sensitivity of the MBL–trade inversion structure to synoptic-scale disturbances over the subtropical Pacific. Cloud droplet effective sizes increase from the coast to open ocean. Furthermore, cloud fraction, cloud-top height, liquid water path, and optical depth all peaked during the morning and reached a minimum by midafternoon.

## 1. Introduction

The stratocumulus (SCu) clouds often observed off the west coast of South America constitute the largest

deck of SCu over subtropical oceans (e.g., Klein and Hartmann 1993), and play an important role in the regional and global climate by substantially reducing the amount of solar radiation absorbed by the ocean (e.g., Hartmann et al. 1992). Coupled ocean–atmosphere models have also shown the potential impact of this cloud deck on the sea surface temperature (SST) and the positioning of the ITCZ over the eastern Pacific (Ma et al. 1996). The SCu cloud amount over the subtropical southeast Pacific (SSEP) exhibits a pronounced dawn-to-afternoon decrease (Minnis and Harrison 1984; Rozendaal 1995), especially during the austral summer [Dec–Jan–Feb (DJF)], when the SCu deck coexists with nearby convection along the central Andes and the Amazon basin. Thus, it has been speculated that diurnally varying divergence–

\*Department of Geophysics, Universidad de Chile, Santiago, Chile.

+Dirección Meteorológica de Chile, Santiago, Chile.

#Atmospheric Sciences, NASA Langley Research Center, Hampton, Virginia.

Corresponding author's address: Dr. René D. Garreaud, Department of Geophysics, Universidad de Chile, Blanco Encalada 2085, Santiago, Chile.

E-mail: rgarreau@dgf.uchile.cl

In final form 25 April 2001.

©2001 American Meteorological Society

convergence originating over the continent (e.g., Gandu and Silva Dias 1998) may contribute to the spatial distribution and diurnal cycle of the marine SCu (Minnis and Harrison 1984; Rozendaal et al. 1995). On the local to regional scale, the coastal strip off southern Peru and northern Chile supports coastal wind-driven upwelling processes responsible for a wealth of economic resources. The alongshore equatorward flow is in turn modulated by a variety of coastally trapped disturbances (Rutllant 1993). Nevertheless, the mean structure and variability of the lower troposphere and the SCu deck over the SSEP are virtually unknown, in contrast to other subtropical regions where major field experiments have been conducted (see Albrecht et al. 1995 for a review). The absence of ground truth also prevents assessing the ability of atmospheric models to diagnose and predict the circulation and cloudiness over this region and validate atmospheric parameters remotely sensed from satellites.

This paper presents preliminary results from meteorological observations taken on board the *R/V Vidal Gormaz* (formerly *R/V Thomas Washington*) along a transect at 27°S from Caldera on the Chilean coast (70°W) to Easter Island (110°W) during the second half of October 1999. The cruise, referred to as CIMAR-5, was organized and supported by the Chilean National Oceanographic Committee (CONA) as part of a multidisciplinary program set up to promote regional marine research. The ship-based meteorological observations (SST, near-surface and upper-air data, cloud-base height) were complemented with large-scale analyses and remotely sensed satellite data to provide a snapshot of the lower troposphere over the SSEP during austral spring.

The meteorological component of CIMAR-5 was undertaken jointly by the Department of Geophysics at the Universidad de Chile (DGF) and the National Meteorological Service (DMC). Its objectives were twofold: to study the mean structure and variability of the lower troposphere over the SSEP, including the marine boundary layer (MBL)-subsidence inversion and the marine SCu, and to assess the overall skill of reanalyses, weather prediction models, and remotely sensed data in representing the atmosphere within an area largely devoid of in situ data. The meteorological data from CIMAR-5 may also be useful for testing MBL parameterizations developed on the basis of data taken in other regions dominated by marine SCu.

The paper is structured as follows. A description of the cruise is presented in section 2. Section 3 provides an overview of the climatological, seasonal, and

synoptic conditions over the southeast Pacific during CIMAR-5. The ship-based observations are analyzed in section 4, while a comparison of these observations with remotely sensed and model data is presented in section 5. A summary of the main findings and an outlook of the research in this area are presented in section 6.

## 2. Cruise description

CIMAR-5 was a shipborne expedition aimed at documenting physical, chemical, and biological aspects of the upper ocean and atmosphere around Easter and Salas y Gomez Islands, about 3500 km west of Chile, and between the coast and these islands. The *R/V Vidal Gormaz* left Caldera (27°05'S, 70°50'W) on 15 October 1999 on the CIMAR-5 cruise. The ship's track is included as part of Fig. 1a. This paper focuses on the first 15 days of the cruise, hereafter referred to as the transect, when the ship was heading to Easter Island (27°10'S, 109°26'W) along 27°S. Minor departures (0.3°) from this latitude occurred during a 6-h visit to San Felix Island (26°18'S, 80°05'W) on 18 October and as the ship approached Easter Island on 28–29 October. During this transect, the ship was stationed at 30 oceanographic locations (stations) for deeper-ocean conductivity-temperature-depth measurements that lasted 2–4 h each. The ship spent 12 days around Easter Island, then moved southeastward to its final destination at Valparaiso (33°02'S, 72°00'W) on 15 November.

The *Vidal Gormaz* was equipped with a standard automatic weather station (AWS), an upper-air sounding system, and a laser ceilometer. Located on the upper deck of the ship [~14 m above sea level (asl)], the AWS recorded air temperature, relative humidity, global solar radiation, atmospheric pressure, and wind speed/direction every 15 s (see Table 1 for details). The AWS operated continuously during the entire cruise, storing 15-min-average values. Ship-relative winds were converted to absolute (earth relative) winds using ship navigation data and compass readings. Global solar radiation was monitored with a LI-COR LI200SZ that, though responding to direct and diffuse radiation between 0.4 and 1.1  $\mu\text{m}$ , was factory calibrated against a full range Eppley Precision Spectral Pyranometer under daylight conditions. Rawinsondes were launched twice daily (0000 and 1200 UTC) from the ship during the transect (16–29 Oct). Additional rawinsondes were launched at

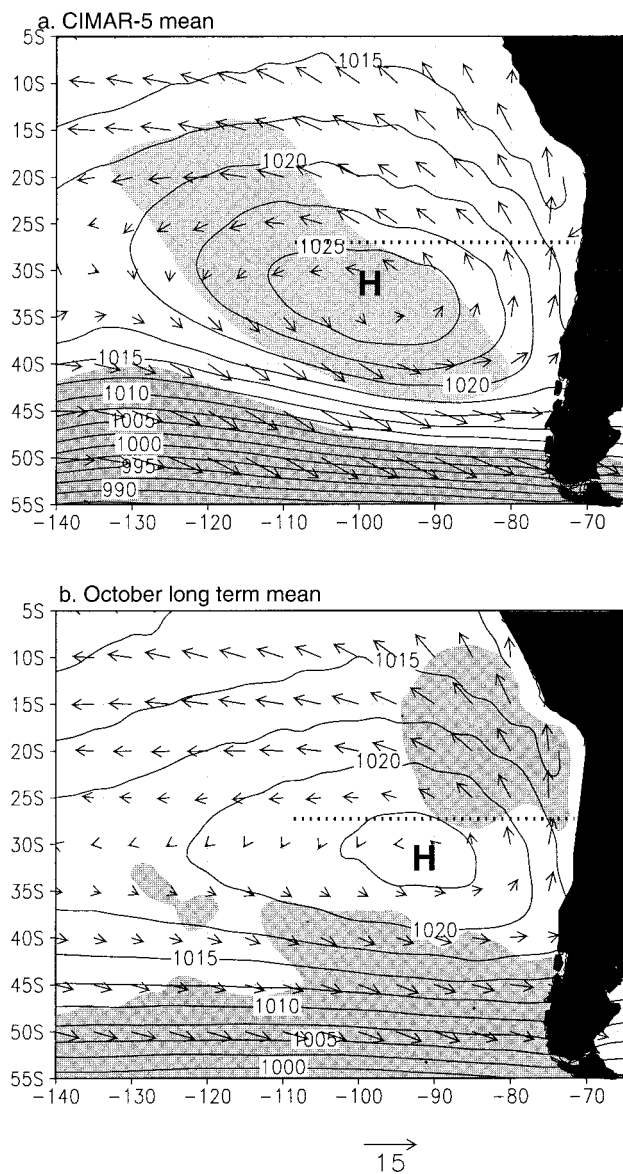


FIG. 1. (a) Mean surface conditions during the CIMAR-5 transect from Caldera to Easter Island (transect period: 16–29 Oct 1999): SLP (contoured every 2.5 hPa), surface winds (reference vector at the bottom of the figure), and SLP anomalies (departures from long-term mean; light shading indicates anomalies in excess of 2 hPa, dark shading indicates *negative* anomalies in excess of -2 hPa). (b) Long-term mean conditions during Oct: SLP (contoured every 2.5 hPa), surface winds (reference vector at the bottom of the figure), and albedo (light shading indicates albedo in excess of 0.4). In both (a) and (b) the dashed straight line indicates ship track during the transect.

1800 UTC on 21, 22, and 23 October. All soundings were made with Vaisala RS80-15G sondes [Global Positioning System (GPS) tracking to derive winds]. The final vertical resolution of the GPS sonde data is about 50 m. The laser (0.904  $\mu\text{m}$ ) ceilometer was also mounted on the ship's upper deck pointing upward,

recording 15-min averages of the estimated cloud-base height for most of the cruise. The zenith low cloud fraction was defined as the ratio of samples with cloud base below 2 km to the total number of samples within a 2-h time window.

In addition to the ship-based observations, imagery from the National Oceanic and Atmospheric Administration's (NOAA) Geostationary Operational Environmental Satellite (*GOES-8*), surface winds from the National Aeronautics and Space Administration's (NASA) QuikSCAT, and numerical model outputs [Medium Range Forecast Model from NCEP, National Centers for Environmental Prediction–National Center for Atmospheric Research (NCEP–NCAR) re-analysis] were collected during CIMAR-5, as detailed in Table 2. Cloud and radiation properties were derived from *GOES-8* for a box consisting of a  $10 \times 10$  array of 4-km pixels centered on the ship location. The satellite data were analyzed with the procedures outlined by Minnis et al. (1995) and Minnis and Smith (1998). The resulting cloud parameters include cloud fraction, cloud-top height, thickness, temperature, phase, effective particle size, optical depth, liquid water path (LWP), top-of-atmosphere (TOA) shortwave (0.2–5.0  $\mu\text{m}$ ) albedo, and outgoing longwave (5–50  $\mu\text{m}$ ) radiation (OLR). The clear-sky quantities are TOA shortwave albedo and OLR, permitting a calculation of the TOA cloud radiative forcing.

### 3. Large-scale conditions

The mean tropospheric conditions off the subtropical west coast of South America are dominated by the subtropical anticyclone, which drives south-southeasterly low-level winds, and a marked temperature inversion, produced by the large-scale subsidence,

TABLE 1. Sensors of the AWS on the R/V *Vidal Gormaz* during CIMAR-5.

Sensor	Type-Model
Wind speed and direction	RM Young 3001
Air temperature and relative humidity	Vaisala HMP-35C
Global solar radiation (direct + diffuse)	LI-COR L1200-S
Barometric pressure	Vaisala PTA-427

TABLE 2. Summary of satellite and numerical model products collected during CIMAR-5.

Product	Time resolution or availability	Pixel or grid spacing	Comments
GOES-8 visible (0.6 $\mu\text{m}$ ) and solar infrared (3.9 $\mu\text{m}$ ) images	1 h	4 km	For clouds and TOA albedo products
GOES-8 infrared (10.8 $\mu\text{m}$ ) and split window (12 $\mu\text{m}$ ) images.	1 h	4 km	For cloud and OLR products
QuikSCAT surface pseudostress	6 h	25 km	Level 3
NCEP-NCAR reanalysis fields	6 h	2.5° × 2.5° lat-long	Fields at mandatory levels (Kalnay et al. 1996)
NCEP-NCAR reanalysis profiles	6 h	2.5° × 2.5° lat-long	Original $\sigma$ levels
MRF-AVN numerical weather prediction fields	3 h	2.5° × 2.5° lat-long	Two daily cycles initialized at 0000 and 1200 UTC

capping a cool atmospheric MBL. In turn, the southerly winds maintain a relatively cold SST due to coastal upwelling and equatorward alongshore advection. The MBL and its capping subsidence inversion support a remarkably persistent deck of SCu, spanning from the coast to about 100°W. The marine SCu over this region reach their maximum coverage during the austral spring [September–October–November (SON)], concurrent with the minimum SSTs off the coast of Peru and northern Chile (Klein and Hartmann 1993). During October, SCu clouds typically occur more than 60% of the time over the region traversed by the ship.

The CIMAR-5 cruise took place during the 1998–2000 La Niña event (Southern Oscillation index, SOI = 0.9 during Oct 1999). Consistently, the South Pacific subtropical anticyclone extended farther to the west and south, driving stronger-than-normal southeasterly trade winds over the southeast Pacific, especially to the west of 90°W (Fig. 1). The average sea level pressure (SLP) along the transect was 2–2.5 hPa above the long-term mean. In contrast with the subtropical region, negative SLP anomalies were observed at midlatitudes over the South Pacific, strengthening

the meridional pressure gradient and zonal flow at around 45°S. Slightly warmer (0.5°C) than average SSTs were observed over open ocean during October 1999, also in connection with La Niña conditions since over the Pacific Ocean subtropical SST anomalies tend to be out-of-phase with those in the Tropics (e.g., Wallace et al. 1998, their Fig. 7c). Air temperature over the SSEP was also warmer than normal, with the largest anomalies (1°C) around 850 hPa, indicative of enhanced large-scale subsidence. On the other hand, the SST along the northern coast of Chile was 0.1–0.7°C colder than average, consistent with slightly stronger than normal alongshore, upwelling-favorable winds.

The synoptic-scale variability during the first 15 days of CIMAR-5 is summarized by longitude–time sections of SLP

and the 500-hPa geopotential height along 27.5° and 45°S (Figs. 2a and 2b), and by synoptic maps at four selected times (Fig. 3). Here we have used NCEP–NCAR reanalysis fields that, as shown in section 4c, agree well with the ship observations over the open ocean. A strong anticyclone was observed at its climatological position during the early and late stages of the transect (Figs. 3a–d). Between 23 and 25 October, the subtropical anticyclone weakened in connection with a midlatitude low pressure cell drifting eastward at 50°S, and subsequently was reinforced by a postfrontal anticyclone (Figs. 3b,c). Also noteworthy during this period is the occurrence of a coastal low in northern Chile (Garreaud et al. 2001), reaching its mature stage on 22 October (Fig. 3c). In spite of these fluctuations, the higher pressures were to the left of the ship during the entire transect to Easter Island, so the ship was always exposed to SSE winds. In the midtroposphere, the subtropical and extratropical circulations were largely decoupled. A subtropical trough moved eastward during the first half of the transect at the same time that a longwave ridge at midlatitudes drifted slowly to the east. The subtropical trough evolved into a cutoff low just to the west of the Andes

by 22 October (Fig. 3b). After 25 October, the subtropical circulation was characterized by a weak ridge drifting westward, concurrent with the passage of a shortwave trough at midlatitudes.

A time–longitude section of the albedo at 27°S from daily (~1700 UTC) *GOES-8* visible imagery is shown in Fig. 2c. The mean westward decrease of albedo is consistent with the climatological decrease of SCu documented on the basis of surface observations (Klein and Hartmann 1993). The synoptic variability in the cloud amount and structure is illustrated by selected visible images in Fig. 4. The anticyclonic conditions during the early part of the cruise were associated with an extensive SCu deck (Fig. 4a). Even at this coarse resolution, the westward (downwind) increase in mesoscale variability of the cloud deck is evident. On 22 October, a wedge of clear skies extended off the coast of central Chile, produced by low-level easterly winds and enhanced subsidence at the southern edge of the surface coastal low/upper cutoff low (Fig. 4b). By 25 October a NW–SE-oriented, active cold front reached southern Chile. The very compact deck of low- and midlevel clouds over much of the subtropical Pacific was likely produced by slow ascent over the prefrontal sector (Fig. 4c). Later, an open-cell cloud pattern dominated the subtropical region, presumably associated with shallow convection as cool, postfrontal air moved over the SSEP (Fig. 4d).

#### 4. Ship-based observations

##### a. Surface observations

Figure 5 shows the time series of several meteorological variables measured at the ship's upper deck level. Figure 5a shows that the subtropical edge of the midlatitude depression and the postfrontal anticyclone have a clear signature on the SLP time series, with a local minimum around 25 October/95°W (the same as the climato-

logical longitude of the high center) followed by anomalous high pressure as the ship approached Easter Island. The surface wind stress ( $\bar{u}|\bar{u}|$ ) reveals a sharp transition from very light winds in the region ahead of the trough axis (days 23–25) to strong southerlies in the postfrontal sector (Figs. 5a,b). The wind data also show a transition of the zonal wind from coastal onshore flow to open-ocean offshore flow at about 500 km from the coastline, presumably a climatological feature.

Air temperature and SST exhibit a parallel, monotonic westward increase (~1.2°C/1000 km), without significant changes as the ship traversed the surface trough (Fig. 5b). While relative humidity was nearly constant at 80% (not shown), the mixing ratio increased from ~8 to 10+ g kg<sup>-1</sup> as the ship moved westward. The moisture change occurred within a day (21 Oct), coincident with the relaxation of the southerly winds, as shown by the time series of dewpoint temperature in Fig. 5b. Moisture convergence ahead

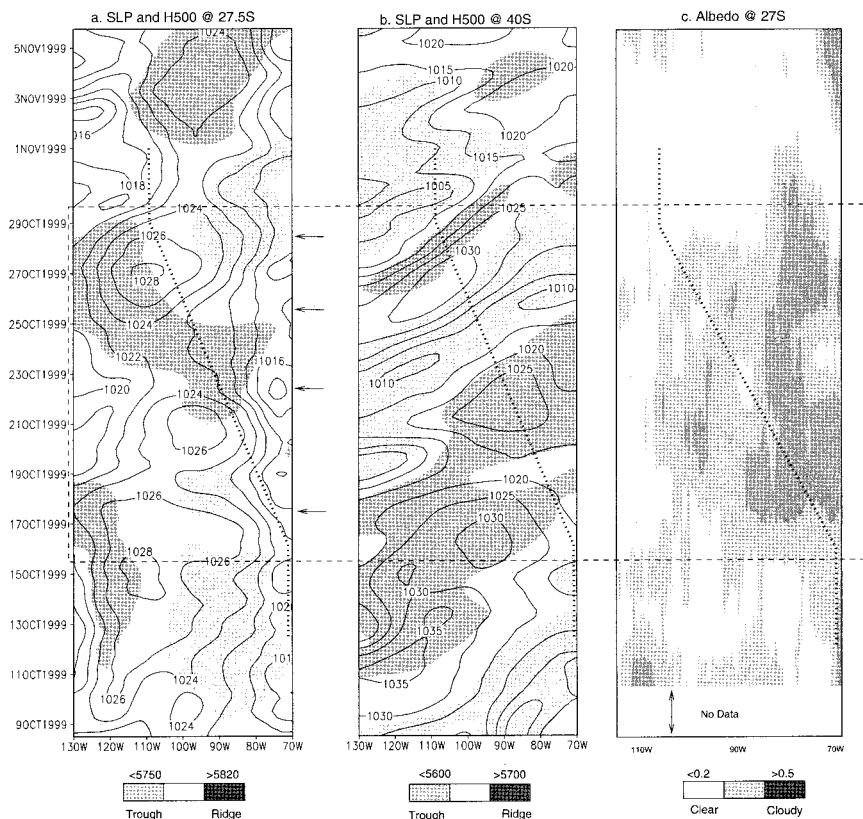


FIG. 2. (a) Time–longitude section along 27.5°S of SLP (contoured every 2 hPa) and 500-hPa height (shaded, shading scale at the bottom). Time increases upward. Dashed box indicates CIMAR-5 transect period. Dotted line indicates ship track. Thin arrows indicate selected times shown in Figs. 4 and 5. (b) As in (a) but at 40°S. Data for (a) and (b) from 6-h NCEP–NCAR reanalysis. (c) As in (a) but for albedo at 27°S (shading scale at the bottom). Data for (c) from *GOES-8* visible images at 1700 UTC.

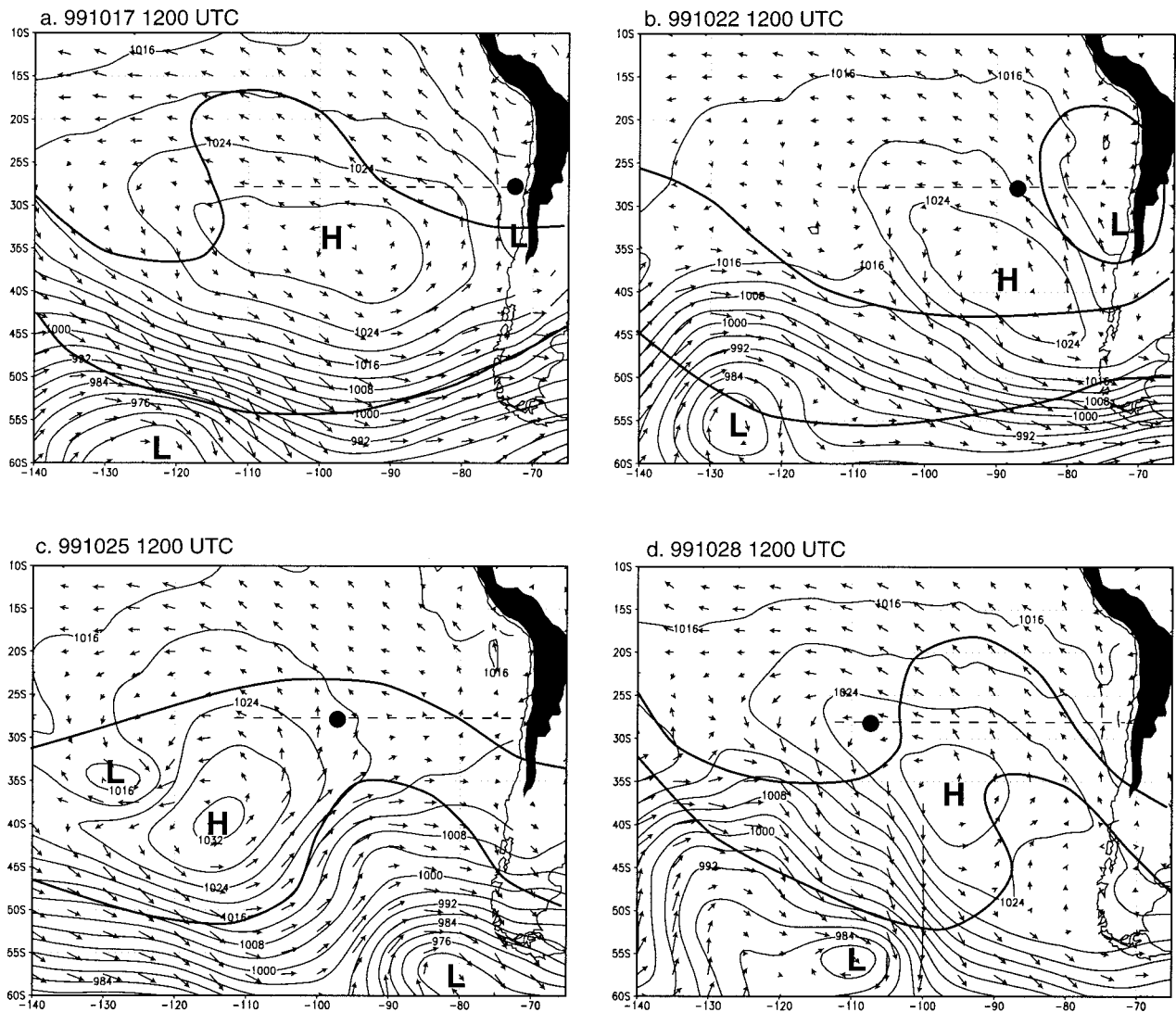


FIG. 3. SLP (contoured every 4 hPa) and surface winds (arrows) at four times during CIMAR-5. Date and hour of the images at the top of each panel. The thick lines are the 5800- and 5500-m geopotential height contours at the 500-hPa level. Data from NCEP–NCAR reanalysis. In (a)–(d) dashed straight line indicates the ship track and circle indicates ship position. Black areas indicate terrain elevation in excess of 2000 m. Maximum wind speed (longest arrow) is  $12.5 \text{ m s}^{-1}$ .

of the surface trough likely contributed to the increase of near-surface moisture on top of the general trend caused by the increase in surface temperature.

During the cruise, the air temperature was  $1^{\circ}$ – $2^{\circ}\text{C}$  cooler than the SST. Bulk estimates of the surface sensible ( $Q$ ) and latent (LE) heat fluxes under this slightly unstable condition (Arya 1988) yield  $LE = 80 \pm 20 \text{ W m}^{-2}$  and  $Q_s = 20 \pm 8 \text{ W m}^{-2}$  (cruise-mean Bowen ratio  $\sim 0.21$ ), where the range is largely caused by the decrease in surface wind during the trough passage. The global solar radiation incident at the ocean surface around local noon fluctuates from  $400 \text{ W m}^{-2}$  during the first half of the transect to  $500 \text{ W m}^{-2}$  during the second half. Assuming a 20%

atmospheric absorption of solar radiation, the TOA SCu albedo would range between 0.45 and 0.55 at noontime. This relatively high albedo is compared with a satellite estimate in section 5a.

#### b. Upper-air data and cloudiness

Figure 6a shows the time–height section of the virtual potential temperature ( $\theta_v$ ) and relative humidity greater than 85%. Most of the rawinsondes reached up to 12 km, but here we show data up to 3 km to focus on the low-level structure. Short-lived fluctuations were eliminated using a 1–2–1 filter in time. The evolution of the lower-tropospheric  $\theta_v$  is dominated by a transient fluctuation around 23 October, superimposed

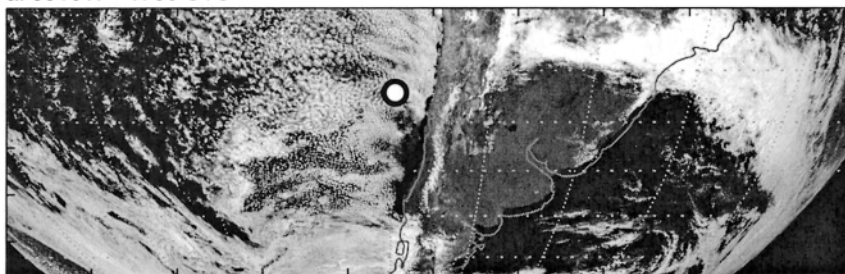
on a steady westward slope of the isentropes. These two features are associated with the midlatitude synoptic perturbation that projected into the subtropical Pacific and the climatological westward slope of the subsidence inversion, respectively, and as such, they are discussed separately.

The depth of the MBL (taken here as the height of the inversion base,  $z_i$ ) increases gradually toward the west (Fig. 6a), from about 600 m at the coast to 1500 m at Easter Island ( $\partial z_i / \partial x \sim 250$  m/1000 km). The westward deepening of the MBL should be produced by the offshore increase of SST (enhanced surface fluxes) and the decrease of the large-scale subsidence. Offshore deepening of the MBL is observed over the eastern boundary of subtropical oceans elsewhere (e.g., Albrecht et al. 1995; Yuter et al. 2000). The inversion layer depth slightly increases westward, from about 150 m at the coast to about 300 m at Easter Island, while the inversion strength (top temperature minus base temperature) remains at about 8°C. The relative humidity exhibits a consistent increase from the surface to the upper part of the MBL (80%→100%) on top of an offshore decreasing trend.

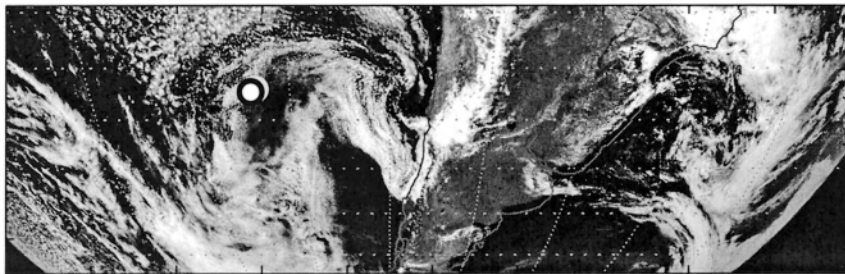
Further insights into the low-level structure along 27°S can be obtained from individual profiles of  $\theta_v$  and water vapor mixing ratio  $q_v$  like those shown in Fig. 7 for four selected times. A relatively shallow ( $z_i \sim 700$ –1000 m), well-mixed, fully coupled MBL was found from the coast well into the open ocean (at least until 90°W—day 25). Over this region the free-atmosphere air is extremely dry ( $q_v < 1$  g kg<sup>-1</sup>; Fig. 7b). To the west of 95°W, the MBL becomes much deeper ( $z_i \sim 1500$  m) and the base of the cloud layer is

signaled by a change in the  $\theta_v$  lapse rate at about 1000 m. At this height, there is also a substantial decrease in moisture, indicative of decoupling between the subcloud and cloud layer (e.g., Bretherton and Wyant 1997). The free-atmospheric air also becomes moister in this region ( $q_v > 3$  g kg<sup>-1</sup>). Such westward increase in moisture above the inversion top also ap-

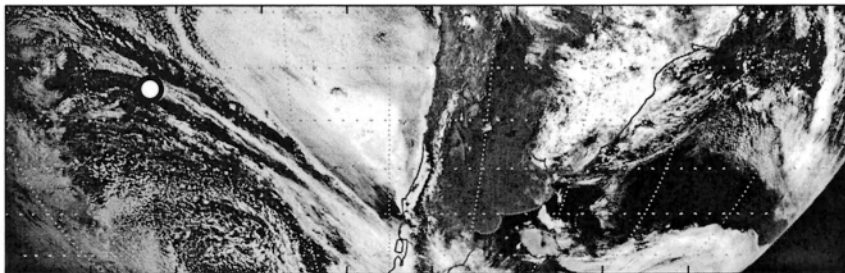
a. 991017 - 1700 UTC



b. 991022 - 1700 UTC



c. 991025 - 1600 UTC



d. 991028 - 1500 UTC

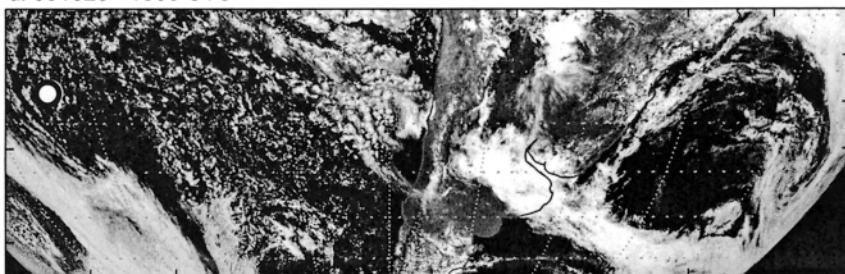


FIG. 4. GOES-8 visible images (0.5  $\mu$ m) at four times during CIMAR-5. Date and hour of the images at the top of each panel. Circles indicate approximate ship position.

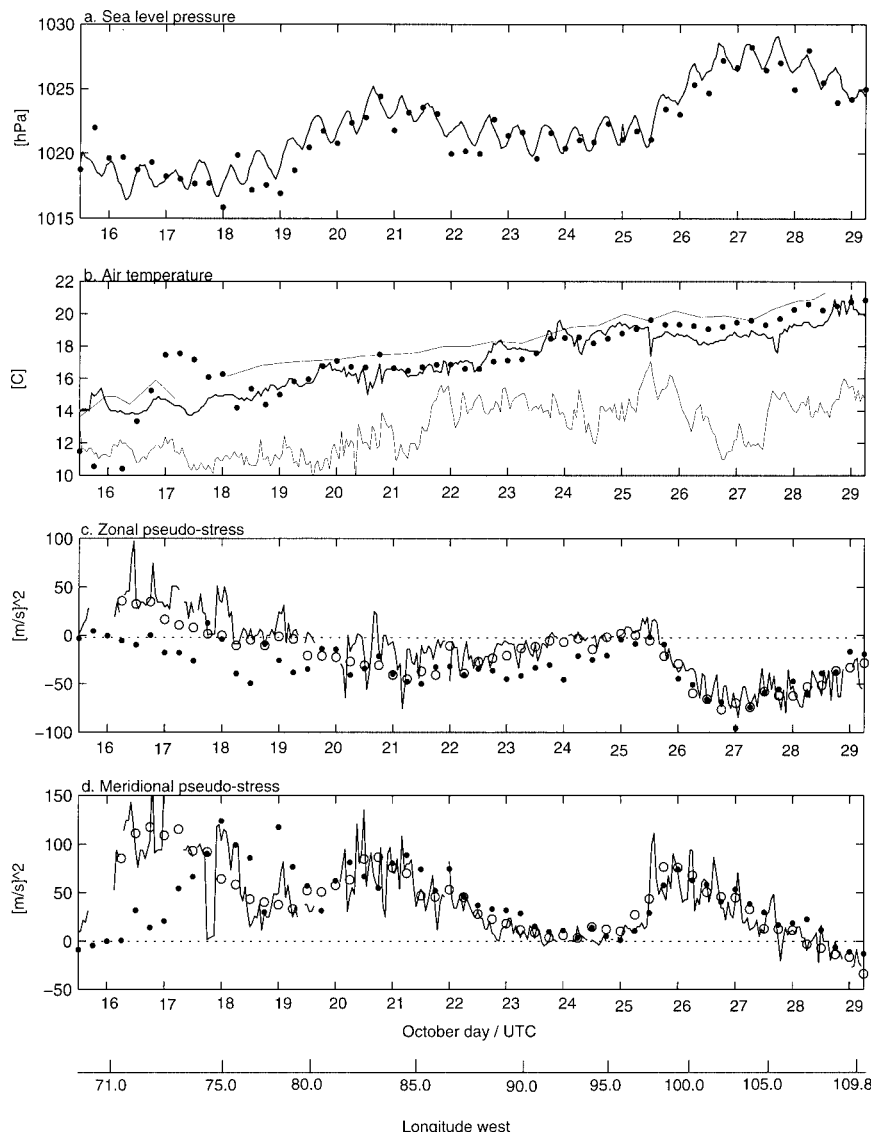


FIG. 5. The 15-min averages of near-surface variables during CIMAR-5 (transect), taken at the ship deck level. (a) Sea level pressure; (b) air temperature (thick line), upper thin line is SST, lower thin line is dewpoint temperature; (c) zonal pseudostress ( $\tau_x$ ); (d) meridional pseudostress ( $\tau_y$ ). In (a)–(d) filled circles are 6-h NCEP–NCAR reanalysis data interpolated to the ship location from reanalysis grid. In (c) and (d) open circles are 6-h QuikSCAT data interpolated to ship location.

pears in the reanalyzed mean profiles (although not as marked as in our data), so we interpret it as a signature of a mean offshore decrement of the large-scale subsidence, rather than synoptic-scale fluctuation. Profiles of the saturated equivalent potential temperatures ( $\theta_{es}$ ) show that the MBL is conditionally unstable ( $\partial\theta_{es}/\partial z < 0$ ) at all longitudes (not shown), but cumulus convection only can occur to the west of  $100^\circ\text{W}$ , where surface air parcels become positively buoyant if raised up to the upper part of the MBL.

Cloud-base height is plotted in Fig. 6b, together with the inversion base and top and the lifting condensation level calculated from the AWS data ( $LCL_s$ ). Two distinctive regimes are evident during the transect. From the coast until  $\sim 93^\circ\text{W}$  (15–24 Oct) the cloud fraction was high (90%–100%) associated with a compact layer of SCu in the top 200–300 m of the MBL. The  $LCL_s$  was consistently near 100 m below the cloud base, presumably because the AWS sampled air within the surface layer. Nevertheless, the  $LCL_s$  closely followed the cloud base, including synchronous high-frequency fluctuations, confirming the coupled character of the MBL during the first half of the transect. In the latter part of the transect ( $95^\circ$ – $110^\circ\text{W}$ ) the cloud fraction was more variable (20%–90%; mean value  $\sim 50\%$ ), and both visual observations at the ship (not shown) and ceilometer data identified small cumuli rising from the base of the cloud layer (coincident with the  $LCL_s$ ) into a patchy, thin layer of SCu at the top of the MBL. Short-lived, scattered showers were observed at three times during this period (Fig. 6b).

Wind speed and direction were rather uniform within the well-mixed MBL from the coast to  $\sim 95^\circ\text{W}$  (Fig. 8a), dominated

by the meridional component ( $\sim +10 \text{ m s}^{-1}$ ) and a lighter and more variable zonal component ( $\sim \pm 3 \text{ m s}^{-1}$ ). The SSE wind decreases substantially within the inversion layer and remains light in the lower free atmosphere (Fig. 8a). In the decoupled MBL regime, the wind structure is more complex (Fig. 8b). The SE flow was almost constant between the surface and the base of the shallow cumulus ( $\sim 600 \text{ m asl}$ ), where it then monotonically decreased up to the inversion base. At and above the inversion layer, winds were typically from the SW with large day-to-day fluctuations in their speed.

## 5. Comparisons with other data

### a. GOES-8 retrievals

The *GOES-8* analyses yield a cruise-mean TOA broadband albedo of  $\sim 0.28$  that undergoes a substantial diurnal variation with means of 0.37 and 0.2 during the morning and afternoon, respectively. The total-sky OLR daytime mean value is  $283 \text{ W m}^{-2}$  compared to  $304 \text{ W m}^{-2}$  for the clear areas. Combining the shortwave and longwave results yields a mean net TOA cloud radiative forcing of  $-72 \text{ W m}^{-2}$ , a value similar to the October 1985 results from Harrison et al. (1990) for the same area. The mean satellite-derived albedo is roughly 30% less than that found off the coast of California during July 1986 (Minnis et al. 1992). The directional (satellite) albedo is also  $\sim 20\%$  less than the global (pyranometer derived) albedo. This difference will need to be resolved, including, perhaps, a recalibration of the onboard pyranometer.

Cloud fraction derived from *GOES-8* is consistent with the ceilometer data; which show mostly overcast skies east of  $95^\circ\text{W}$  and decreasing cloud amounts to the west. Cirrus clouds were observed over the SCu along the transect only during 18 October. Cloud-top heights were derived with two approaches using the retrieved cloud-top temperature  $T_c$ . The first method (Minnis et al. 1992) uses the difference between SST and  $T_c$  and an assumed MBL lapse rate  $\Gamma_{BL} = -7.1^\circ\text{C km}^{-1}$  to yield the lapse rate height  $z_r = (SST - T_c) / \Gamma_{BL}$ . The second, more conventional, technique simply searches the nearest rawinsonde sounding to match  $T_c$  to an altitude  $z_{RS}$  by starting at the surface and proceeding upward. Figure 9a compares the results of the two methods with the inversion base height  $z_i$  from the rawinsondes. Up to 25 October ( $95^\circ\text{W}$ ),  $z_r$  and  $z_{RS}$  are generally within 200 m of  $z_i$  and vary in the same manner. The greatest differences be-

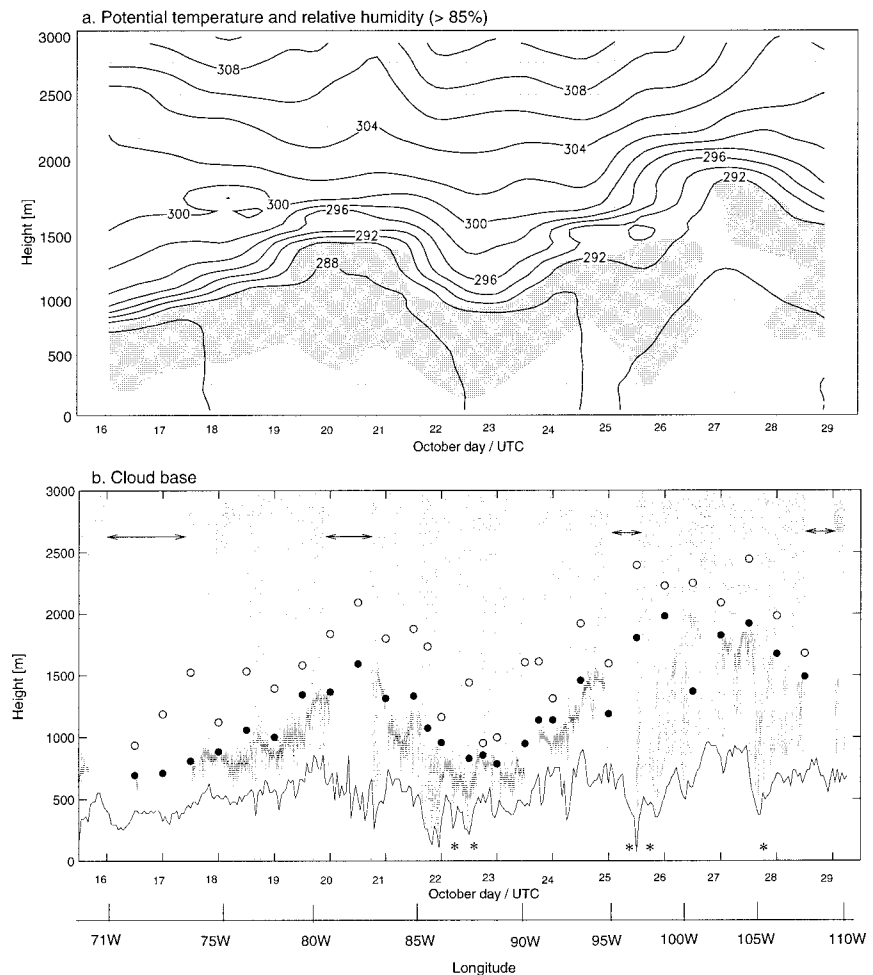


FIG. 6. (a) Time–height section of the potential temperature during CIMAR-5 (transect) from 12-h radiosondes. Data were smoothed using a 1-2-1 filter in time. Shading indicates relative humidity in excess of 85%. (b) Cloud-base height from 30-min laser ceilometer during CIMAR-5 (transect). Horizontal arrows at the top indicate periods with no ceilometer data. Also shown are the top (open circles) and the base (solid circles) of the trade inversion derived from 12-h radiosondes, and the lifting condensation level (solid line) from 15-min near-surface observations. Asterisks denote observations of light, scattered showers.

tween  $z_{RS}$  and  $z_r$  occur on 22 and 26 October. In the former case, the value of  $T_c$ ,  $9^\circ\text{C}$ , cannot be found in the sounding at altitudes below 2800 m, while in the latter, the value of  $T_c$ ,  $0.3^\circ\text{C}$ , is only found around 4000 m. The temperature at the inversion level of 829 m at 1200 UTC, 22 October was  $10.3^\circ\text{C}$ . Cloud-base height during the morning of 26 October is near 2000 m, well above  $z_i$  but below the top of the inversion. A second inversion was found at 2050 m, but the temperature was  $1.5^\circ\text{C}$ , too warm to match  $T_c$ . Thus, cloud heights are estimated better with  $z_r$  than with  $z_{RS}$  during both days.

Several phenomena may lead to these discrepancies between the sounding and observed cloud temperatures. Mahesh et al. (1997) found that the response

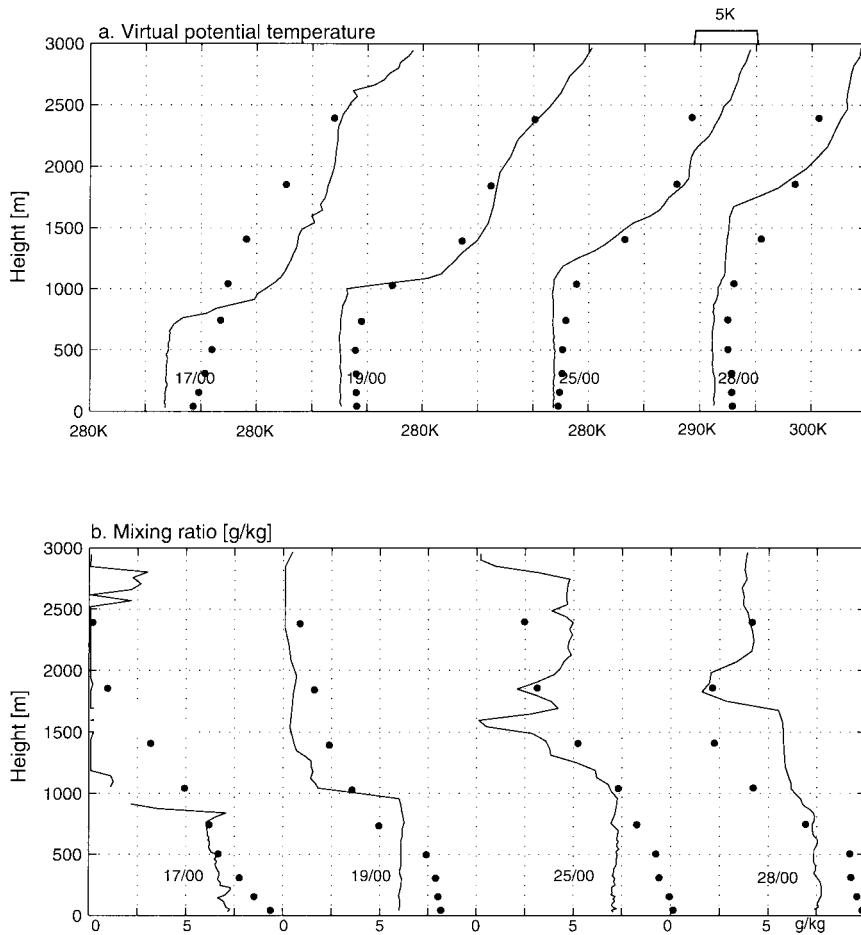


FIG. 7. (a) Vertical profiles of virtual potential temperature ( $\theta_v$ ) at four times during CIMAR-5. Sounding time is indicated by day (Oct)/UTC at the side of each profile. Dots are values of  $\theta_v$  from the NCEP–NCAR reanalysis (original  $\sigma$  levels) interpolated to the ship position. (b) As in (a) but for mixing ratio.

time of the rawinsonde thermistors can often cause errors in the temperatures around steep inversions. The sounding resolutions on 22 and 26 October were 63 and 93 m, respectively, around the cloud top, while the corresponding temperatures increased by  $2.4^\circ$  and  $3.5^\circ\text{C}$ . Thus, the soundings may not have had sufficient resolution or the thermal lag smeared out the actual inversion-base temperature. The observed cloud temperature is derived from a model that includes infrared scattering, which may decrease the observed temperature to a value colder than the actual cloud temperature. The correction may not have been large enough to account for all of the scattering resulting in an underestimate of  $T_c$ . The discrepancies may be a result of all of these factors. In any case, the soundings lacked the cloud temperatures at the appropriate heights. It follows from this discussion that larger errors in  $z_{\text{RS}}$  will occur if the original sounding resolu-

tion is not used. In many cases,  $T_c$  corresponds exactly to the inversion base, so any resolution reduction could eliminate the possibility of placing the cloud below the inversion in the sounding method. This is especially true for operational retrievals that use model reanalyses like NCEP that may not accurately resolve MBL inversions (see below). Overall, it may be concluded that the lapse rate method is more accurate and robust for determining the cloud top for low- and midlevel clouds over the subtropical oceans.

Daily mean values of cloud droplet effective radius  $r_e$  and optical depth  $\tau$  are plotted in Fig. 9b. The droplet size is lowest near the coast and gradually increases to the west and then fluctuates between 11 and  $19\ \mu\text{m}$ . Presumably, the near-coastal values of approximately  $9\ \mu\text{m}$  result from larger concentration of aerosols in this area compared to the pristine marine air. The compact cloud layer between the coast and  $75^\circ\text{W}$  may also play a role in reducing cloud droplet size because the droplets have

less time to grow as they ascend to the cloud top. Beyond  $75^\circ\text{W}$ , the MBL is less likely to be influenced by continental air and the clouds would be expected to have larger droplets to the west as seen in Fig. 9b. The largest values of  $r_e$  exceed  $17\ \mu\text{m}$  and correspond to some of the times when scattered showers were observed. In that more pristine part of the transect (west of  $75^\circ\text{W}$ ), the mean optical depth and effective radius are negatively correlated with  $\tau$  explaining 50% of the variance in  $r_e$ . Mean optical depth from *GOES-8* for the cruise is 6.4, a value 42% less than that observed by Minnis et al. (1992) off the California coast. This optical depth difference explains the albedo differences noted above between the clouds observed during the transect and those observed by Minnis et al. (1992).

Many of the *GOES-8* cloud parameters also varied diurnally. Cloud fraction, cloud-top height, LWP, and optical depth all peaked during the morning and

reached a minimum by midafternoon. Table 3 shows the mean values of  $r_e$ ,  $z_T$  and  $\tau$  for the entire transect at 3 h. The mean optical depth was nearly a factor of 3 higher during the early morning than during the afternoon while mean cloud-top height decreased by approximately  $30 \text{ m h}^{-1}$ . The maximum mean value of  $r_e$ ,  $17.1 \mu\text{m}$ , also occurred during the morning. On average, the mean value was relatively constant at  $16 \mu\text{m}$  during the remainder of the day.

The nature of the diurnal cycles was somewhat different east of  $95^\circ\text{W}$  compared to that west of  $95^\circ\text{W}$ . Although the phases of the diurnal cycles were similar, cloud amount and cloud-top height varied more erratically to the west than in the more compact cloud deck to the east. For example, Fig. 10 shows the variations in  $z_T$  and  $\tau$  for two portions of the transect. In the eastern segment (18–19 Oct), the hour-to-hour variability in cloud-top height (Fig. 10a) is much less than that seen in Fig. 10c for observations near Easter Island. Presumably, this difference is a result of the more frequent occurrence of smaller-scale cumuli forming within the deeper boundary layer in the west compared to the more compressed boundary layer in the east. The cloud fraction in the west tends toward zero during the afternoon, while the clouds appear to thin out more often than breaking up in the eastern sector. Optical depths (Figs. 10b and 10d) follow similar patterns in both sectors except that the clouds in the west tend to start the day thinner than those in the east resulting in the dissipation of the clouds during the afternoon in the deeper boundary layer. The difference in the cloud diurnal cycle is also seen in the insolation. The ratio of afternoon-to-morning insolation is 1.3 during 18–19 October and only 1.1 during 26–27 October.

#### b. NCEP–NCAR reanalysis and QuikSCAT winds

Figure 5 shows the ship-based surface observations (SLP,  $T_a$ ,  $u$ , and  $v$ ) together with the correspond-

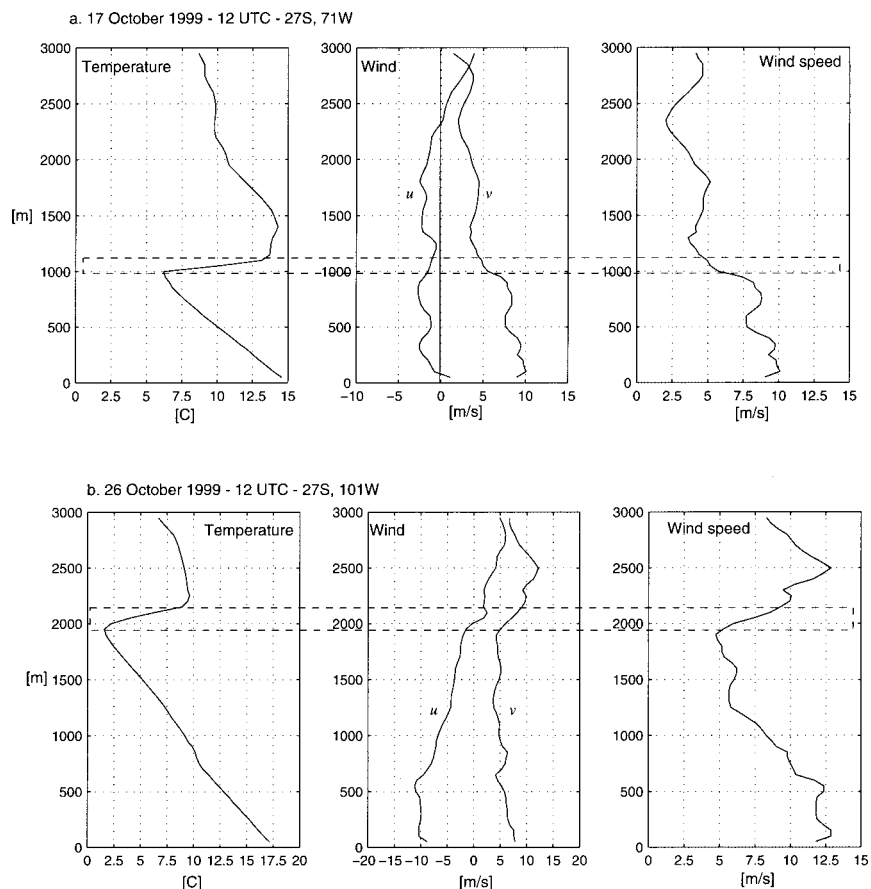


FIG. 8. (a) Vertical profiles of temperature (left), zonal and meridional wind components (middle), and wind speed (right) at 17 Oct 1999, 1200 UTC. Dashed rectangle indicates inversion layer. (b) As in (a) but at 26 Oct 1999, 1200 UTC.

ing 6-h NCEP–NCAR reanalysis values (Kalnay et al. 1996). The latter were obtained by bilinear interpolation of the  $2.5^\circ \times 2.5^\circ$  latitude–longitude fields to the ship position. West of  $75^\circ\text{W}$  (about 500 km off the coast), there is a remarkable agreement between the ship observations and the reanalysis data [linear correlation coefficient in excess of 0.9 for all variables; error rms:  $\text{rms}(T_a) = 0.9^\circ\text{C}$ ,  $\text{rms}(\text{SLP}) = 0.9 \text{ hPa}$ ,  $\text{rms}(u) = 2.8 \text{ m s}^{-1}$ ,  $\text{rms}(v) = 1.9 \text{ m s}^{-1}$ ]. This agreement is especially significant considering the absence of in situ data over this region (neither surface data nor upper-air data collected from the ship were placed into the Global Telecommunications System during the cruise). The reanalysis pressure, temperature, and meridional wind are unbiased, and they capture the general westward trend as well as the amplitude and timing of the synoptic-scale disturbance. Of course, the point-value, near-instantaneous measurements taken at the ship deck contain significant high-frequency variability not resolved by the temporally and spatially averaged reanalysis values.

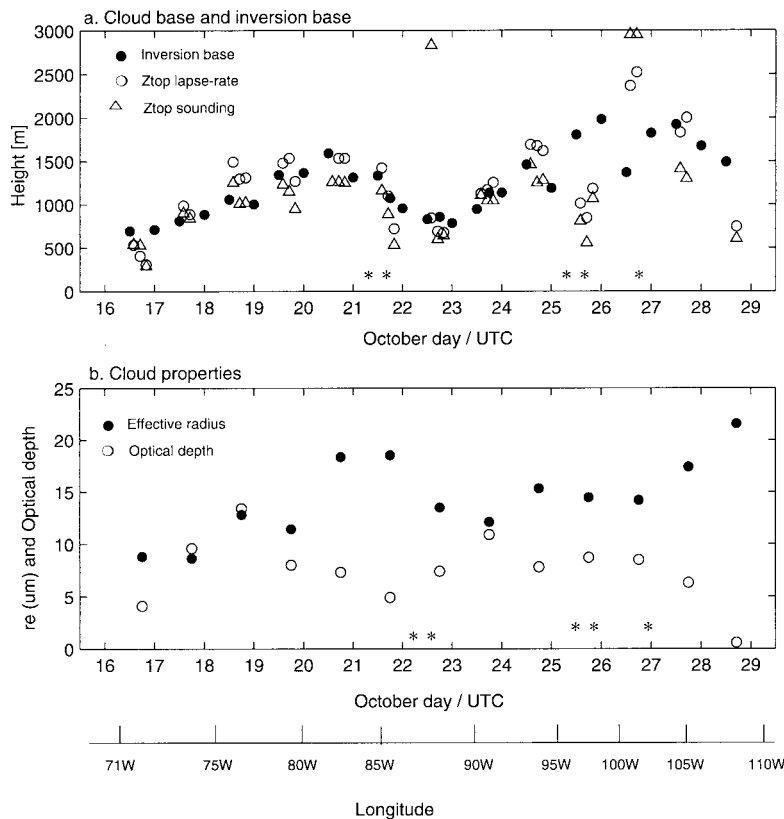


FIG. 9. Cloud properties derived from *GOES-8* during CIMAR-5 (transect). (a) Cloud-top height derived from *GOES-8* using the lapse rate method (open circles) and the sounding method (triangles). Also shown is the inversion base derived from the 12-h radiosondes (filled circles). (b) Mean daytime cloud droplet effective radius (closed circles) and optical depth (open circles). Asterisks denote observations of light, scattered showers.

The zonal wind shows an easterly bias (except during the last part of the cruise), but closely follows the observed data. Similar results were found when comparing ship data and the interpolated model outputs from the NCEP MRF up to 48 h of lead time (not shown).

In contrast to the open ocean, the reanalysis values show little agreement with the ship observations

TABLE 3. Mean daytime cloud properties derived from *GOES-8* during CIMAR-5 (transect period: 16–28 Oct 1999).

Parameter	1400 UTC	1700 UTC	2000 UTC
Effective radius ( $\mu\text{m}$ )	17.1	15.8	16.1
Cloud top (m)	1230	1190	1100
Optical depth	12.0	5.8	4.8

over the coastal strip ( $72^{\circ}$ – $75^{\circ}\text{W}$ ), except for SLP. The coarse grid spacing and topography employed in the reanalysis-associated model likely caused this problem, since the model coastline is about 300 km away from the actual coastline at  $27^{\circ}\text{S}$ . The use of the incorrect surface type over the coastal strip causes a large, diurnally varying bias in the reanalysis temperature, humidity, and winds.

Figures 5c and 5d also include the 10-m pseudostress wind components ( $ulul, vlvl$ ) derived from the NASA's QuikSCAT (QuikSCAT winds). Here we have used the Florida State University Center for Ocean–Atmospheric Prediction Studies (FSU–COAPS) Objectively Analyzed Pseudostress available every 6 h on a  $1^{\circ} \times 1^{\circ}$  latitude–longitude grid. The fields are produced from the QuikSCAT swath data level 3 (25-m footprint) interpolated onto a regular grid using a variational approach (Legler et al. 1998; Pegion et al. 2000). The gridded QuikSCAT pseudostress was bilinearly interpolated to the ship position. Despite the differences in the time and space averaging involved in each estimate of the near-surface wind, there is remarkable agreement between the ship-based and QuikSCAT winds.

Both zonal and meridional QuikSCAT components are unbiased and have an rms error less than  $0.8 \text{ m s}^{-1}$  with respect to the 6-h-averaged ship data. The validity of the QuikSCAT winds over the coastal strip ( $71.5^{\circ}$ – $75^{\circ}\text{W}$ ) is also noteworthy.

Figure 11 shows the 500-hPa geopotential height from (interpolated) reanalyses and rawinsondes. The reanalyses capture the overall evolution ( $r = 0.83$ ), with values in close agreement with those observed (error rms = 25 mgp). Similar results were found at other mid- and upper levels. We also were able to use the NCEP–NCAR reanalysis profiles of temperature and mixing ratio in the original sigma levels, bilinearly interpolated to the ship position. The derived  $\theta_v$  and  $q_v$  are plotted in Fig. 7 together with the observed profiles at four selected times. With the exception of the sounding within the coastal region, the reanalysis profiles capture the essential features of the lower troposphere. These features are, however, not at all evident when using mandatory pressure levels. Furthermore,

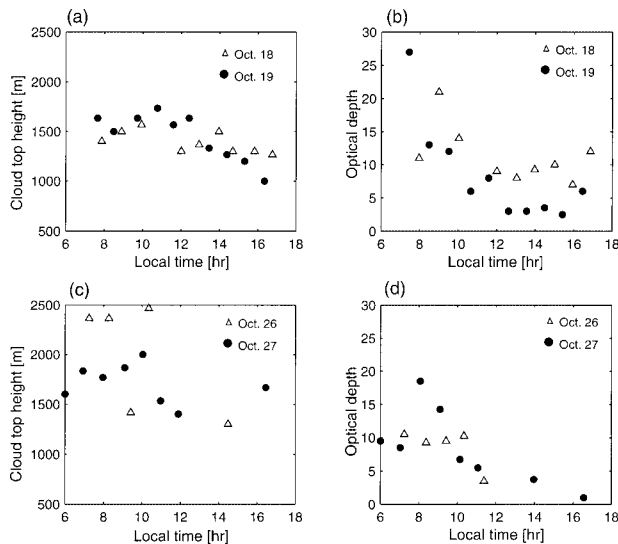


FIG. 10. (a) Cloud-top height derived from *GOES-8* using the lapse rate method for 18 and 19 Oct ( $75^{\circ}$ – $78^{\circ}$ W). (b) Satellite derived optical depth for 18 and 19 Oct. (c) As in (a) but for 26 and 27 Oct ( $99^{\circ}$ – $103^{\circ}$ W). (d) As in (b) but for 26 and 27 Oct.

reanalysis profiles exhibit a small warm bias and a large wet bias within the MBL, with potential problems for the representation of low clouds and the use of such reanalyses for interpreting satellite data over this region as discussed earlier.

## 6. Summary and outlook

Ship-based surface and upper-air data taken along a transect at  $27^{\circ}$ S from the Chilean coast ( $71.5^{\circ}$ W) to Easter Island ( $109.8^{\circ}$ W) during the second half of October 1999 have been used to provide an in situ description of the lower troposphere over the subtropical southeast Pacific. Remote sensing results from analyses of *GOES-8* data supplement the shipborne measurements to provide a more complete description of the troposphere during the cruise. While many details in the measurements are associated with the particular synoptic- and large-scale (La Niña event) conditions during the cruise, the observations reveal some basic, but largely unknown, aspects over this region as well as con-

firming that the characteristics of the marine boundary layer here are similar to those over other regions. Our main findings are as follows:

- SST and near-surface air temperature increased gradually westward (about  $4^{\circ}\text{C}$  in 4000 km), with air temperature consistently about a degree colder than SST. Near-surface relative humidity remained nearly constant at  $\sim 80\%$  along the transect.
- The moisture in the lower and midtroposphere above the inversion top increased from very dry conditions near the coast ( $q < 0.5 \text{ g kg}^{-1}$ ) to moister conditions near Easter Island ( $q \sim 4 \text{ g kg}^{-1}$ ), indicative of an offshore decrease in large-scale midtropospheric subsidence.
- Consistent with the two points above, the MBL evolves gradually from a shallow, well-mixed MBL topped by a compact deck of SCu close to the coast; to a deeper, decoupled MBL with cumuli rising into patchy SCu near Easter Island, in a similar fashion to that documented over eastern boundaries of other subtropical oceans. The passage of a relatively weak synoptic-scale disturbance over the subtropical Pacific leads to marked changes in the depth of the MBL and low-level circulation, indicative of a great sensitivity of the subtropical MBL-trade inversion structure to synoptic-scale perturbations.
- Cloud-top height and base as well as cloud fraction vary diurnally with maximum values during the morning and minima during the afternoon. Cloud droplet effective sizes increase from the

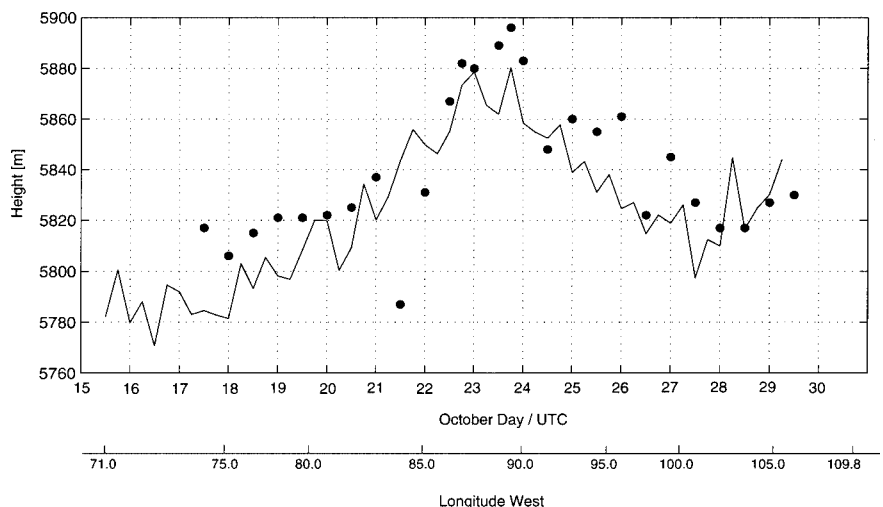


FIG. 11. 500-hPa geopotential height during CIMAR-5 (transect). Filled circles are values from twice-a-day radiosondes. Solid line is the 6-h values from NCEP–NCAR reanalysis interpolated to the ship position.

coast to open ocean, presumably due to the offshore decrease in aerosol concentration within the MBL. Cloud optical depth and liquid water path have a significant diurnal cycle, varying, on average, by more than a factor of 2 each day.

- Satellite-derived cloud-top heights using a lapse rate technique and QuikSCAT surface wind are in good agreement with ship-based observations along the entire transect. Over open ocean (about 500 km away from the coastline) there is also a good agreement between NCEP–NCAR reanalysis and ship-based data. The use of data at standard pressure levels, however, smears much of the low-level vertical structure, and the NCEP–NCAR reanalysis profiles are generally moister than observed. Along the coastal strip, the reanalyzed wind, temperature, and humidity fields are significantly different from the observed values, presumably due to systematic errors.

The results presented here provide only a brief summary of data taken during the first half of CIMAR-5. Detailed measurements from the ship as well as large-scale satellite datasets and reanalyses from both segments of the experiment (available from the authors) should provide a wealth of information on the SE Pacific for modeling and observational studies. The key role of the subtropical deck of SCU on regional and global climate, as well as the coastal circulation on regional weather, warrant the realization of further field experiments and enhancement of the long-term observational network over the southeast Pacific. It is expected that the data gathered during this cruise will help in the design of these future efforts.

*Acknowledgments.* We want to thank the effort in organization and funding provided by the Chilean National Oceanographic Committee (CONA), the efficiency of the R/V *Vidal Gormaz* crew, and the dedication of the technician from the National Weather Service (DMC), Mr. José Nuñez, in maintaining the equipment on board. Dr. Bruce Albrecht kindly provided the laser ceilometer from the University of Miami. Credit is also due to the Program in Atmospheric Dynamics and Climate (PRODAC) and to the Department of Geophysics (DGF), both at the Universidad de Chile and to the DMC for facilities and additional funding. Thanks are also due to Drs. James O'Brien and Mark Bourossa at FSU–COAPS, and Dr. Michael Freilich (OSU) for providing the QuikSCAT data for the cruise period. Gridded NCEP–NCAR reanalysis data were obtained through the NOAA Climate Diagnostics Center. Sigma level NCEP–NCAR reanalysis data were kindly provided by Dean Vickers from Oregon State University (OSU). Valuable comments were provided by Chris Bretherton and an anonymous reviewer. R. Bustos and Z. Salinas kindly helped in

processing the cruise data. The satellite analyses were supported by the NOAA Office of Global Programs Pan American Climates Studies Interagency Agreement NA99AANGR0204. Thanks to David Young, NASA Langley, and Kirk Ayers, AS&M Inc., for their assistance with the satellite analysis.

## References

- Albrecht, B. A., M. P. Jensen, and W. J. Syrett, 1995: Marine boundary layer structure and fractional cloudiness. *J. Geophys. Res.*, **100** (D7), 14 209–14 222.
- Arya, S. P. S., 1988: *Introduction to Micrometeorology*. Academic Press, 303 pp.
- Bretherton, C. S., 1992: A conceptual model of the stratocumulus-trade cumulus transition in the subtropical oceans. Proc. *11th Int. Conf. on Clouds and Precipitation*, Montreal, PQ, Canada, Int. Commission on Clouds and Precipitation and Int. Association of Meteorology and Atmospheric Physics, 374–377.
- , and M. C. Wyant, 1997: Moisture transport, lower tropospheric stability, and decoupling of cloud-topped boundary layers. *J. Atmos. Sci.*, **54**, 148–167.
- Gandu, A. W., and P. L. Silva Dias, 1998: Impact of the tropical heat sources on the South American tropospheric circulation and subsidence. *J. Geophys. Res.*, **103**, 6001–6015.
- Harrison, E. F., P. Minnis, B. R. Barkstrom, V. Ramanathan, R. D. Cess, and G. G. Gibson, 1990: Seasonal variation of cloud radiative forcing derived from the Earth Radiation Budget Experiment. *J. Geophys. Res.*, **95**, 18 687–18 703.
- Hartmann, D. L., M. E. Ockert-Bell, and M. L. Michelsen, 1992: The effect of cloud type on earth's energy balance: Global analysis. *J. Climate*, **5**, 1281–1304.
- Kalnay, E., and Coauthors, 1996: The NCEP/NCAR 40-Year Reanalysis Project. *Bull. Amer. Meteor. Soc.*, **77**, 437–471.
- Klein, S. A., and D. L. Hartmann, 1993: The seasonal cycle of low stratiform clouds. *J. Climate*, **6**, 1587–1606.
- Legler, D. M., M. A. Bourassa, A. D. Rao, and J. J. O'Brien, 1998: NSCAT surface wind fields using optimally tuned direct minimization techniques. Preprints, *Ninth Conf. on Interaction of Sea and Atmosphere*, Phoenix, AZ, Amer. Meteor. Soc., 32–35.
- Ma, C., C. R. Mechoso, A. W. Robertson, and A. Arakawa, 1996: Peruvian stratus clouds and the tropical Pacific circulation: A coupled ocean–atmosphere GCM study. *J. Climate*, **9**, 1635–1645.
- Mahesh, A., V. P. Walden, and S. G. Warren, 1997: Radiosonde temperature measurements in strong inversions: Correction for thermal lag based on an experiment at the South Pole. *J. Atmos. Oceanic Technol.*, **14**, 45–53.
- Minnis, P., and E. F. Harrison, 1984: Diurnal variability of regional cloud and clear-sky radiative parameters derived from GOES data. Part II: November 1978 cloud distributions. *J. Appl. Meteor.*, **23**, 1012–1301.
- , and W. L. Smith Jr., 1998: Cloud and radiative fields derived from *GOES-8* during SUCCESS and the ARM-UAV Spring 1996 Flight Series. *Geophys. Res. Lett.*, **25**, 1113–1116.
- , P. W. Heck, D. F. Young, C. W. Fairall, and J. B. Snider, 1992: Stratocumulus cloud properties derived from simulta-

- neous satellite and island-based instrumentation during FIRE. *J. Appl. Meteor.*, **31**, 317–339.
- , and Coauthors, 1995: Cloud optical property retrieval (Subsystem 4.3). Clouds and the Earth’s Radiant Energy System (CERES) algorithm theoretical basis document, Vol. III: Cloud analyses and radiance inversions (Subsystem 4), CERES Science Team, Eds., NASA Rep. 1376, 135–176.
- Pegion, P. J., M. A. Bourassa, D. M. Legler, and J. J. O’Brien, 2000: Objectively derived daily “winds” from satellite scatterometer data. *Mon. Wea. Rev.*, **128**, 3150–3168.
- Rozendaal, M. A., C. B. Leovy, and S. A. Klein, 1995: An observational study of diurnal variations of the marine stratiform clouds. *J. Climate*, **8**, 1795–1809.
- Rutllant, J. A., 1993: Coastal lows and associated southerly winds events in north-central Chile. Preprints, *Fourth Int. Conf. on Southern Hemisphere Meteorology and Oceanography*, Hobart, Australia, Amer. Meteor. Soc., 268–269.
- Wallace, J. M., E. M. Rasmusson, T. P. Mitchell, V. E. Kousky, E. S. Sarachick, and H. von Storch, 1998: On the structure and evolution of ENSO-related climate variability in the tropical Pacific: Lessons from TOGA. *J. Geophys. Res.*, **103** (C7), 14 241–14 259.
- Yuter, S. E., Y. Serra, and R. A. Houze Jr., 2000: The 1997 Pan American Climate Studies Tropical Eastern Pacific Process Study. Part II: Stratocumulus region. *Bull. Amer. Meteor. Soc.*, **81**, 483–490.

